
A fast horizon detector and a new annotated dataset for maritime video processing

Yassir Zardoua¹ · Mohammed Boulaala² · Mhamed El Mrabet² · Abdelali Astito¹

Abstract Accurate and fast sea horizon detection is vital for tasks in autonomous navigation and maritime security, such as video stabilization, target region reduction, precise tracking, and obstacle avoidance. This paper introduces a novel sea horizon detector from RGB videos, focusing on rapid and effective sea noise suppression while preserving weak horizon edges. Line fitting methods are subsequently employed on filtered edges for horizon detection. We address the filtering problem by extracting line segments with a very low edge threshold, ensuring the detection of line segments even in low-contrast horizon conditions. We show that horizon line segments have simple and relevant properties in RGB images, which we exploit to suppress noisy segments. Then we use the surviving segments to construct a filtered edge map and infer the horizon from the filtered edges. We propose a careful incorporation of temporal information for horizon inference and experimentally show its effectiveness. We address the computational constraint by providing a vectorized implementation for efficient CPU execution, and leveraging image downsizing with minimal loss of accuracy on the original size. Moreover, we contribute a public horizon line dataset to enrich existing data resources. Our algorithm's performance is rigorously evaluated against state-of-the-art methods, and its components are validated through ablation ex-

periments. Source code and dataset files are available at: <https://drive.google.com/drive/folders/...>

Keywords Horizon line · Sea-sky line · Real-time execution · Vectorized computations · Maritime video processing · Annotated dataset

1 Introduction

1.1 The maritime horizon: definition and applications

The maritime horizon, also referred to as the sea-sky line in some cases, is defined as the boundary line that separates the sea region from the region immediately above it (as shown in Fig. 1) [1–3]. We should note that in maritime images depicting mountains or coastlines, as illustrated in Fig. 1(b), the horizon according to the maritime video processing literature is the line separating the mountain from the sea [1, 4–8]. This maritime horizon is semantically distinct from the wild horizon literature, which addresses the non-linear boundary separating the mountain from the sky [9, 10].

Our paper focuses on detecting the maritime horizon line in RGB images, which, as highlighted in [8], offer richer daytime information at a lower cost compared to infrared images. This sea horizon plays a pivotal role in intelligent and autonomous sea navigation [1, 8]. Previous studies have demonstrated that correctly detecting the maritime horizon provides significant benefits to video processing systems, such as digital video stabilization [11–13], improved target detection and tracking [4, 14], reduced search region [15–17], and obstacle avoidance [18–20]. These studies include commercial surveillance systems like ASV@ (Automatic Sea Vision) [21], which integrate the sea horizon detector. Survey [3] reports a strong trade-off between robustness and computational load. Therefore, further research in this specific field is necessary

Yassir Zardoua (**Corresponding author**)
E-mail: yassirzardoua@gmail.com

Mohammed Boulaala
E-mail: m.boulaala@gmail.com

Mhamed El Mrabet E-mail: m.elmrabet@gmail.com · Abdelali Astito
E-mail: abdelali_astito@yahoo.com

¹ Smart Systems & Emerging Technologies, FSTT, Abdelmalek-Essaadi University, Tetouan, Morocco

² Industrial Systems Engineering and Energy Conversion Team, FSTT, Abdelmalek-Essaadi University, Tetouan, Morocco



Fig. 1: The horizon line separates the sea from the sky (a) and the sea from the coast (b)

1.2 Literature review

In this section, we succinctly discuss an extensive set of horizon detection algorithms. We recommend that readers refer to surveys [1, 3, 8] for an in-depth literature analysis.

Gershikov et al. [22] detect one horizon point per column as the pixel with the maximum vertical edge response. The final horizon is fit on these points using the least-squares technique, which is known for its high sensitivity to outliers. Better algorithms project edge maps to another space favoring the appearance of the horizon as a peak. The first attempt in this context was conducted by Bao et al. [23]. They detected image edges using LoG (Laplacian of Gaussian) and extracted the horizon using the global maximum of the transformed space. The horizon may not correspond to the global maximum due to image noises. Therefore, Zhang et al. [24] enhanced the work in [23] by analyzing three geometric features of local peaks of the transformed space. These features assume that noisy edges have high scatter, which is unsuitable for line-up sea clutter. Similar to [23], Schwendeman and Thomson [12] detected the horizon as the global peak of the Hough space and suggested a contrast-based quality metric to remove faulty global peaks. Authors of [12] report that their method is susceptible to lighting changes, one of the main factors degrading horizon edges. Like [12], Lie et al. [9] employed a Canny edge detector with an automatic threshold to extract the weak horizon edges while minimizing the noise. Subsequently, they identified the horizon using a dynamic programming technique to infer the curved horizon from the extracted edges. While they reported good results on low-contrast horizon of non-maritime images, the effectiveness of this methodology in our case has yet to be evaluated.

Many researchers have observed that directly inferring the horizon from extracted edges often leads to incorrect detections, primarily due to high texture in RGB images [1, 3]. As a result, they have incorporated various edge filtering

techniques to enhance clutter suppression while preserving horizon edges. In this context, Shen et al. [25, 26] proposed an adaptive size of the Gaussian kernel to avoid excessive suppression of horizon edges. The size is established based on the image resolution, specifically the number of rows. Regardless of the Gaussian kernel's window size, it consistently weakens the horizon edges due to the kernel's built-in smoothing effect, reducing high-frequency components in the image.

The authors of [22, 27] have discovered that morphological erosion is more effective in preserving weak horizon edges compared to Gaussian filters. In response to this, Li et al. [6] recently introduced a more advanced morphological filter that calculates the reconstruction by erosion of the edge response. This filter operates under the assumption that maritime clutter in RGB images typically manifests as blobs, such as sun glints on the sea surface or small waves. This assumption allows the filter to effectively preserve horizon edges, which do not appear as blobs. However, the iterative nature of the erosion-based reconstruction technique, even when applied to downsized images, impacts its processing speed.

Numerous researchers have conducted extensive investigations into the utility of median filters. These filters have garnered attention for their superior performance compared to Gaussian filters, primarily due to their capacity to preserve intensity gradients without excessive smoothing. Median filters, with odd-sized pixel windows, prevent the creation of intermediate intensities that could weaken the transition across the horizon edge. They achieve this by ranking pixel intensities and selecting the central value, preserving a sharp transition across the horizon line [28].

To increase the suppression effect, it is better to use multiple median windows of increasing size instead of one large median filter [29]. This is known as the multi-scale median filter, an approach that has produced some of the best results in the maritime literature [23, 30–33]. In alignment with this

approach, Prasad et al. [31] applied five median scales and transformed the result into a Hough space where the voting rule is modified to favor longer edges. Such a process is resource-greedy and takes tens of seconds per frame. A similar and faster alternative applies ten median scales [30] and detects horizon candidates from each scale using the vertical edge response and the standard Hough transform. The final candidate is selected using a goodness score based on the strength and colinearity of its edges. Instead of detecting candidate lines on each median scale, Jeong et al. [32] significantly reduced the computational load of the multi-scale median filter by processing only one weighted edge map, which they computed by averaging the edges of each median scale. They conducted experiments that demonstrated this approach's significantly improved accuracy and remarkable speed enhancement, being 90 times faster than the methods presented in [30] and [31]. Overall, multi-scale median filtering [32] and the sophisticated morphological filter [6] reported the best ability to preserve weak horizon edges.

Dong et al. [5] proposed a novel filter that effectively removes sea noise while detecting horizon lines with weak edges. They addressed computational speed concerns by extracting a region of interest (ROI) encompassing the horizon. Line segments were subsequently extracted from the ROI using an adaptive local threshold. The authors of this filter conducted experiments to demonstrate that the distribution of gradient angles along horizon line segments is significantly higher than that of the noise. Therefore, they stretched the line segments by a factor of 0.5, filtered them based on the stability of their gradient angles, and applied a RANSAC algorithm to obtain the horizon line. The same reference [5] justifies the 0.5 stretching by explaining that the horizon line segments will further span along the horizon, thereby enhancing their gradient angle stability while reducing the stability for noisy segments. This filtering approach effectively preserved weak horizon edges and outperformed median-scale filters [30, 32]. However, its applicability to our case is questionable because this algorithm was designed based on the unique properties of infrared imagery, which significantly differ from RGB images, as detailed in [1, 8]. For example, studies in [1, 5] point out that the infrared texture on the sea surface is poorer compared to RGB images. This characteristic is advantageous for streamlining the filtering process since higher texture levels tend to introduce more noisy segments.

Another category of algorithms incorporates regional properties such as pixel intensities and texture, which are usually fused with edge-based features to improve the accuracy and computational load; for instance, Jeong et al. [32] process only a region of interest extracted through analysis of color distribution difference of multiple sub-images. Other methods exploit the color properties of the sky to detect it and assume that the horizon is the linear boundary

right below it [34, 35]. Such assumption easily breaks on images depicting coastal regions (as in Fig. 1(b)), where the horizon is the boundary separating the coast from the sea rather than the sky class. Ettinger et al. [36] and Fefilatyev et al. [14] consider the horizon as the line maximizing the intra-class variance of the two regions split by that line, which requires expensive computations even on low-resolution images. Liang and Liang [7] significantly enhanced the speed and accuracy of this approach by processing color and texture information in two small patches sliding along the considered Hough candidate.

Simple assumptions about the color and texture of maritime semantic classes lead to failures even for machine learning-based algorithms, such as SVM (Support Vector Machine), decision trees [37], and GMM (Gaussian Mixture Model) [15, 38]. For instance, authors of [38] train a GMM where the feature vector of each class (sea, coast, and sky) is supposed to have a Gaussian distribution, which is unsuitable due to the non-homogeneity of image classes (details in [3]). The machine learning paradigm has also been investigated on non-maritime images, where the horizon is represented as a non-linear boundary separating ground and sky pixels; learning-based methods such as [39, 40] process only image patches centered at Canny edge pixels. Classifying all Canny edge pixels without applying a proper filter is time consuming, especially if we lower the edge detection threshold for extracting weak horizon edges. The edge classification approach was quickly adopted for maritime images by Jeong et al. [33], who demonstrated that using a convolutional neural network outperformed traditional classifiers and handcrafted features [39, 40]. To reduce computational load, they processed the input image with the multi-scale median filter from [32], employing two additional scales to limit the number of candidate edge pixels and speed-up the classification process. While the study in [33] reports excellent CNN performance on a wide range of maritime images, we found that the excessive use of median filtering scales suppresses not only weak horizon edges but also those with higher edge magnitudes. Therefore, the horizon detector in [33] is limited to horizon lines with prominent edges.

1.3 Main contributions and paper structure

Previous and recent research consistently underscores the essential role of edge information in accurately detecting the horizon line [1, 5, 8, 33]. The analysis in Section 1.2 and survey [3] suggest that the current literature would greatly benefit from a horizon detector that meets two critical criteria: (1) high robustness against sea clutter while preserving weak horizon edges and (2) efficient CPU execution

with minimal computations¹. Accordingly, we categorize our contributions into algorithmic and dataset contributions. We summarize our algorithmic contributions in the following four points:

- We introduce a novel filter that generates a filtered edge map, preserving very weak horizon edges while suppressing various forms of sea clutter. This filtered edge map is then used for horizon line inference.
- In the line inference stage, we propose an outlier handler model (OHM) that effectively incorporates temporal information to avoid outlier detections.
- We enhance the computational efficiency by vectorizing the filtering processes.
- We effectively leverage image downsizing for faster computations by accurately projecting the detected horizon from the downsized image to the original size.

Our dataset contribution involves the public sharing of 18 video clips, totaling over 6,000 frames, which we meticulously annotated for the maritime horizon line. This dataset introduces multiple new scenarios to enhance and complement the most extensive video dataset currently available, the Singapore Maritime Dataset (SMD), initially introduced in [1].

The remainder of this paper is structured as follows: Section 2 describes the proposed algorithm, Section 3 introduces the new dataset and compares it with other datasets, Section 4 ablates and validates the components of our algorithm and compares it with relevant methods, and Section 5 concludes the work and suggests future research.

2 Algorithm

We will provide an overview of the proposed algorithm before detailing its stages. We show the overall algorithm pipeline in Fig. 2. We note that the main ideas we employed in stages 2 and 3 (see Fig. 2) were introduced in the recent survey [3] as a promising research direction. The study in [3] motivated these ideas after examining the horizon line segment properties in 85 RGB images with challenging sea clutter. Stage 1 extracts the red channel² of the input image $I_{rgb}(x, y)$ and applies a Line Segment Detector (LSD) algorithm to detect the set of line segments S^a . The key process is to select from S^a candidate horizon segments (CHSs), which are more likely to correspond to the horizon line. We denote CHSs by set S^f . We rely on two filtering stages in establishing set S^f : the length-slope filter (LSF) and the region of interest filter (ROIF) (see Fig. 2). The LSF selects from S^a

two sets of segments, S^c and S^d , which contain the longest segments with a slope less than a threshold α_{th} . We directly consider segments of set S^c as CHS, i.e., $S^c \subset S^f$, because they are all longer than segments of set S^d . The ROIF establishes one tight region of interest (ROI) that encompasses each segment of set S^c . Subsequently, a segment of set S^d is selected as an additional CHS only if encompassed by at least one of the defined ROIs. We denote segments satisfying such a condition by S^e . We denote the set containing all CHSs by S^f , which is equal to $S^c \cup S^e$. Stage 4 establishes the filtered edge map $E(x, y)$ as pixels along each segment of set S^f . Finally, stage 5 infers the horizon using line-fitting techniques and temporal information.

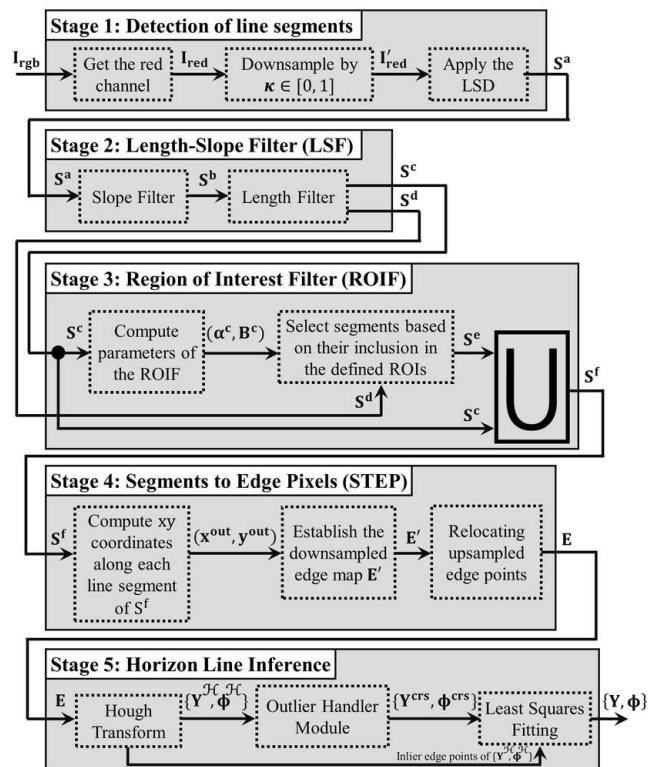


Fig. 2: Pipeline of our method

2.1 Detection of line segments

Our method detects and evaluates image line segments instead of whole lines to create a filtered edge map $E(x, y)$ with relevant horizon edges. The use of line segments provides numerous benefits. First, we gain more robustness against partial occlusions of the horizon (e.g., by ships). Such occlusion significantly changes horizon properties in occluded regions, making the latest full-line detectors ineffective against simple occlusions, as highlighted in [3]. Second, line segments are inherently efficient scale-invariant

¹ The reader can find a discussion on the importance of criteria (2) in survey [3]

² We applied the LSD on 9 color channels on a wide range of sea images, visually analyzed the results, and concluded that the red channel produced the best results

descriptors [41] and can be shared with other components of the system for efficient video processing. Third, as we will show in Sections 2.2 and 2.3, horizon line segments exhibit simple and relevant properties on a wide range of cluttered RGB images. Fourth, detecting line segments is an old problem, and the current literature offers several fast and robust algorithms with sub-pixel accuracy [42, 43].

In this paper, we detect line segments using the fast Line Segment Detector (LSD) developed by Von Gioi et al. [42], which combines the advantages of its antecedents while significantly limiting their inconveniences. We exploit its following properties to create a robust and fast horizon edge filter: not misled by faulty segments induced by highly textured regions thanks to the gradient angle; a significant decrease of the false positives and negatives related to fixed detection thresholds; adopts a novel criterion selecting both long and short segments; satisfying linear-time execution. As shown in Fig. 2, we extract the red channel and down-sample it by $\kappa \in]0, 1[$. Applying the LSD on the downsampled red channel I'_{red} reduces the computational time and mitigates the negative effect of high-frequency components. Throughout this paper, we denote an unknown set of segments u by S^u , its number of elements by N^u , and the v -th segment of set S^u by $S^{u,v}$. Thus, we can express a given set u as $S^u = \{S^{u,v}\}_{v=1:N^u}$. Given this notation, we refer to segments output by the LSD by $S^a = \{S^{a,i}\}_{i=1:N^a}$. Figure 3(b) shows that despite the weak edge response of the horizon (see Fig. 3(a)), set S^a contains enough horizon segments to allow its detection. We explain this result by the relative stability of gradient angles on the horizon, which allows the LSD [42] to grow longer segments on the horizon even when it is blurred. We favor such a possibility by setting for the LSD a small gradient magnitude threshold³.

2.2 Length-Slope Filter (LSF)

2.2.1 Description and motivation

The LSF (stage 2 in Fig. 2) filters segments of set S^a using their slope and length. In our case, the EO sensor is mounted on terrestrial moving platforms whose deviation is much smaller than aerial-based platforms. Therefore, we suppress too tilted line segments, which may lead to detecting false sea horizons when they are remarkably long. Several factors can induce too-tilted segments, such as the vehicle's wakes depicted by the rear camera or the long vertical edges (e.g., antennas) of nearby ships. Therefore, the LSF first filters out segments of set S^a according to the slope condition of equation 1:

$$S^{a,i} \in S^b \text{ if } |\alpha^{a,i}| \leq \alpha_{th} \quad (1)$$

³ To be precise, we talk about the lowest hysteresis threshold

where $|\cdot|$ is the absolute value, $\alpha^{u,v}$ denotes the slope of segment $S^{u,v}$, α_{th} is a scalar threshold, and S^b is the set of segments satisfying the slope condition. It is tempting to fix α_{th} to a minimal value (e.g., $\alpha_{th} = 0.09$), but this can remove valuable horizon segments because, as reported in previous works [1, 14, 38], cameras onboard small sea platforms (e.g., buoys, USVs) may incur non-negligible deviations when facing sea winds and waves. We further filter segments of set S^b by removing the relatively shorter segments. Concretely, segment $S^{b,j}$ will survive the filter only if it is among the longest N^c segments of set S^b . We formally express this condition in equation 2:

$$S^{b,j} \in S^c \text{ if } L^{b,j} \geq L_{srt}^{b,N^c} \quad (2)$$

where S^c is the set containing survived segments, $L^{u,v}$ is the length of the v -th segment $S^{u,v}$, N^c is a scalar threshold specifying the number of the longest segments to select⁴, and $L_{srt}^{u,v}$ is the length (in pixels) of the v -th-longest segment of set S^u ⁵. The underlying assumption of the filtering condition of equation 2 is that pixels of the horizon line will ideally have the same gradient orientation value, which allows the LSD to group horizon pixels into the lengthiest segments. In contrast, pixels of the most common sea clutter (e.g., sea waves, sunglints, wakes) will correspond to scattered gradient orientations. In light of this, Fig. 3(b) shows that despite a large number of line segments on the sea surface, most are shorter than the few segments detected on the horizon. Hence, we perform no further filtering on segments of set S^c and consider them as horizon segments, i.e., $S^c \subset S^f$ (see the output of stage 3 in Fig. 2). Figure 3(c) shows segments of set S^c for $N^c = 15$. We explain in Section 2.3 that settling for set S^c as the only horizon segments could lead to missing valuable horizon segments due to some factors affecting the stability gradient orientations of horizon pixels. Therefore, we select more segments by taking the next longest N^d segments from set S^b as expressed in equation 3:

$$S^{b,j} \in S^d \text{ if } L_{srt}^{b,N^c} > L^{b,j} \geq L_{srt}^{b,N^{d'}} \quad (3)$$

where $N^{d'} = N^c + N^d$ and N^d is a scalar threshold that corresponds to the number of segments in set S^d ($N^d \gg N^c$; e.g., $N^d = N^c \times 10$). Unlike set S^c , we do not directly consider segments in set S^d as horizon segments because their length is relatively close to that of noisy segments, as shown in Fig. 3(d). The next stage captures additional horizon segments from set S^d using information extracted from set S^c .

⁴ N^c is also the number of elements (segments) in set S^c .

⁵ For instance, $L_{srt}^{b,1}$ is the length value of the longest segment in set S^b

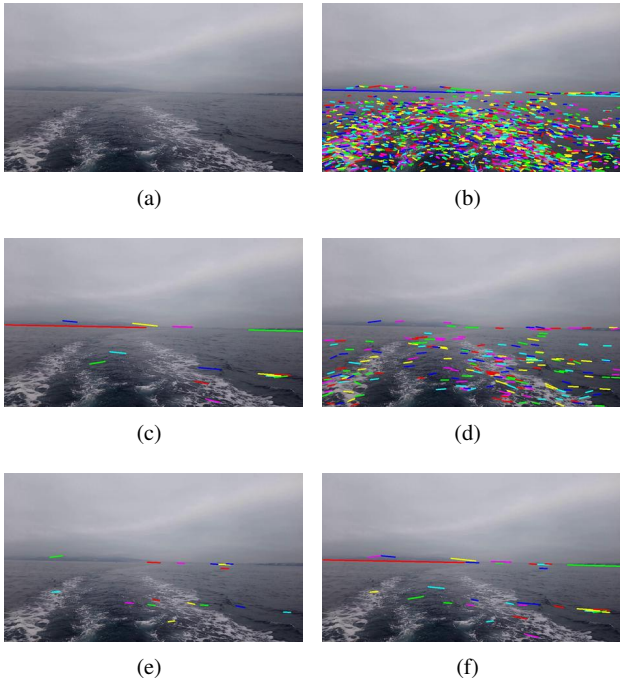


Fig. 3: Intermediate results of line segments filtering: (a) original image; (b) segments of set S^a ; (c) segments of set S^c ; (d) segments of set S^d ; (e) segments of set S^e ; (f) segments of set S^f

2.2.2 LSF: implementation details

We denote Cartesian coordinates of the starting point and ending point⁶ of the v -th segment $S^{u,v}$ of set S^u by $p_s^{u,v} : (x_s^{u,v}, y_s^{u,v})$ and $p_e^{u,v} : (x_e^{u,v}, y_e^{u,v})$, respectively. Thus, we denote x_s^u, x_e^u, y_s^u , and y_e^u as vectors containing coordinates of segments of set S^u :

$$\begin{aligned} x_s^u &= [x_s^{u,1}, x_s^{u,2}, \dots, x_s^{u,N^u}]^T \in \mathbb{R}^{N^u \times 1} \\ x_e^u &= [x_e^{u,1}, x_e^{u,2}, \dots, x_e^{u,N^u}]^T \in \mathbb{R}^{N^u \times 1} \\ y_s^u &= [y_s^{u,1}, y_s^{u,2}, \dots, y_s^{u,N^u}]^T \in \mathbb{R}^{N^u \times 1} \\ y_e^u &= [y_e^{u,1}, y_e^{u,2}, \dots, y_e^{u,N^u}]^T \in \mathbb{R}^{N^u \times 1} \end{aligned} \quad (4)$$

There are two processes to vectorize in the LSF: the slope-based (equation 1) and length-based (equations 2 and 3) filtering conditions. The former starts by computing vector α^a according to equation 5:

$$\begin{aligned} \alpha^a &= [\alpha^{a,1}, \alpha^{a,2}, \dots, \alpha^{a,N^a}]^T \in \mathbb{R}^{N^a \times 1} \\ &= (y_e^a - y_s^a) \oslash (x_e^a - x_s^a) \end{aligned} \quad (5)$$

where α^u is the vector corresponding to the slopes of segments in S^u and \oslash is the Hadamard (component-wise) division. All filtered sets of segments in this paper, i.e., S^b, S^c ,

⁶ We arbitrarily consider that the starting point is always on the left of the ending point.

S^d, S^e , and S^f , represent subsets of set S^a and are thus established by a vectorized indexing; concretely and generally, we use the different filtering conditions (e.g., equations 1 and 2) to establish vector $I_{u',u} \in \mathbb{R}^{N^{u'} \times 1}$, whose values are indices that would obtain the filtered set $S^{u'}$ by indexing set S^u . We will see in Section 2.3.4 that vector $I_{u',u}$ also allows obtaining attributes of a given set $S^{u'}$ from homologous attributes of one of its supersets S^{u7} , avoiding thus redundant computations. Using discussed indexing, we get segments of set S^b by establishing vector $I_{b,a} \in \mathbb{R}^{N^b \times 1}$, whose values are indices of slopes $\alpha^{a,i}$ (see equation 5) satisfying the condition expressed in equation 1. Eventually, we index set S^a by vector $I_{b,a}$ to produce the desired set S^b . As set S^c and S^d are established based on the length of segments of set S^b , we first compute a length vector according to equation 6:

$$\begin{aligned} L^b &= [L^{b,1}, L^{b,2}, \dots, L^{b,N^b}]^T \in \mathbb{R}^{N^b \times 1} \\ &= \left((x_e^b - x_s^b)^{\odot 2} - (y_e^b - y_s^b)^{\odot 2} \right)^{\odot 1/2} \end{aligned} \quad (6)$$

where $L^{u,v}$ is the length of the v -th segment $S^{u,v}$ and \odot is the Hadamard (element-wise) power. Then, we establish vector $I_{srt}^{L^b} \in \mathbb{R}^{N^b \times 1}$ whose values are indices that would sort values of L^b from highest to lowest. Thus, vector $I_{c,b}$, whose elements are indices of set S^b satisfying equation 2, is established by slicing the first N^c elements of vector $I_{srt}^{L^b} \in \mathbb{R}^{N^b \times 1}$. Similarly, we get vector $I_{d,b}$, whose elements are indices of set S^b satisfying equation 3, by slicing $I_{srt}^{L^b}$ from the $(N^c + 1)$ -th element to the $(N^c + 1 + N^d)$ -th element. Eventually, we get set S^c and S^d by indexing set S^b using vectors $I_{c,b}$ and $I_{d,b}$, respectively.

2.3 Region Of Interest Filter (ROIF)

2.3.1 Motivation and assumption

We mentioned in Section 2.2 that taking the longest N^c segments from set S^b could miss valuable line segments. This issue is fundamentally caused by certain types of noise, such as the Gaussian noise of low-quality sensors and the poor horizon contrast. Such noise disturbs the gradient orientation of horizon pixels, thus hindering the LSD from growing long segments on the horizon line. Fig. 3(d) shows that the low contrast condition led to growing short segments on the horizon. The same disturbed property, i.e., gradient orientation, provides the key to mitigating this issue; we assume that, unlike noisy segments, short horizon segments have a much higher colinearity with longer horizon

⁷ For instance, we can get the slope vector $\alpha^{u'}$ by indexing α^u with vector $I_{u',u}$.

segments. Figure 4(a) depicts a synthetic example of this assumption. We show the result of using this assumption on the real image in Fig. 3(a); Fig. 3(e) shows that additional horizon segments, denoted as set S^e , are successfully captured from S^d . Selecting more horizon segments from S^d often leads to capturing more noisy segments, as shown in Fig. 3(e). However, having more horizon segments allows more performance, as we will experimentally show in Section 4.5.

2.3.2 The filtering condition: initial formulation

We aim in this Section to formulate an initial expression of the filtering condition based on the colinearity assumption we mentioned in Section 2.3.1 and illustrated in Fig. 4(a). To this end, we define one region of interest, denoted as $\mathcal{R}^{c,k}$, to encompass the k -th segment $S^{c,k}$. Subsequently, we consider that the l -th segment $S^{d,l}$ is an additional horizon segment only if both of its endpoints fall in at least one and the same region $\mathcal{R}^{c,k}$. Figure 4(b) shows an example of the filtering regions corresponding to Fig. 4(a) in pink. Figure 4(c) shows in yellow the segments of set S^d satisfying the condition we just mentioned. We initially formulate this condition in equation 7:

$$S^{d,l} \in S^e \text{ if } \exists k : \left((p_s^{d,l} \in \mathcal{R}^{c,k}) \wedge (p_e^{d,l} \in \mathcal{R}^{c,k}) \right) = 1 \quad (7)$$

where S^e is the set grouping additional horizon segments selected from set S^d , $p_s^{d,l}$ and $p_e^{d,l}$ are the starting and ending point of segment $S^{d,l}$, respectively, \in is the inclusion operator, \wedge is the logical *and*, and 1 is the true Boolean.

2.3.3 Mathematical development of equation 7

Implementing the filtering condition in equation 7 first requires further mathematical development. This breaks down to verifying that a given endpoint of segment $S^{d,l}$ is included in a given region $\mathcal{R}^{c,k}$. We execute this task in four steps: (1) set the width (thickness) $W_{\mathcal{R}}$ of all regions $\mathcal{R}^{c,k}$ to an arbitrarily small value; (2) define function $g^{c,k}(x)$ as the linear curve crossing both endpoints $p_s^{c,k}$ and $p_e^{c,k}$ of segment $S^{c,k}$; (3) compute $\forall h \in \{s, e\}$ the quantity $d_h^{k,l}$, which is the normal distance from point $p_h^{d,l}$ to line $g^{c,k}(x)$; (4) consider that $p_h^{d,l} \in \mathcal{R}^{c,k}$ only if $d_h^{k,l} < t_{roi}$, where $t_{roi} = \frac{W_{\mathcal{R}}}{2}$ is the parameter controlling the width $W_{\mathcal{R}}$. We eventually express the developed filtering condition equivalent to equation 7 in equation 8, where quantity $d_h^{k,l}$ is computed using equations 9 and 10:

$$S^{d,l} \in S^e \text{ if } \exists k : \left((d_s^{k,l} \leq t_{roi}) \wedge (d_e^{k,l} \leq t_{roi}) \right) = 1 \quad (8)$$

$$\begin{aligned} d_h^{k,l} &= \frac{1}{\sqrt{1 + (\alpha^{c,k})^2}} \times |g^{c,k}(x_h^{d,l}) - y_h^{d,l}|; \forall h \in \{s, e\} \\ &= \frac{1}{\sqrt{1 + (\alpha^{c,k})^2}} \times |\alpha^{c,k} \times x_h^{d,l} + \beta^{c,k} - y_h^{d,l}| \end{aligned} \quad (9)$$

$$\begin{aligned} \beta^{c,k} &= y_s^{c,k} - \alpha^{c,k} \times x_s^{c,k} \\ &= y_e^{c,k} - \alpha^{c,k} \times x_e^{c,k} \end{aligned} \quad (10)$$

where $\alpha^{c,k}$ and $\beta^{c,k}$ correspond to the slope and intercept of curve $g^{c,k}(x)$, respectively. Note that $\alpha^{c,k}$ is equal to the slope of the k -th segment $S^{c,k}$ and can be obtained from vector α^a .

2.3.4 Implementation details

We present in this Section the details to vectorize the filtering condition we developed in equation 8. We define matrix \mathbb{D}_h to contain $\forall (k, l)$ the quantities $d_h^{k,l}$. We illustrate \mathbb{D}_h in equation 11 and compute it using equation 12:

$$\mathbb{D}_h = \begin{bmatrix} d_h^{1,1} & d_h^{1,2} & \dots & d_h^{1,N^d} \\ d_h^{2,1} & d_h^{2,2} & \dots & d_h^{2,N^d} \\ \vdots & \vdots & \ddots & \vdots \\ d_h^{N^c,1} & d_h^{N^c,2} & \dots & d_h^{N^c,N^d} \end{bmatrix} = (d^{k,l}) \in \mathbb{R}^{N^c \times N^d} \quad (11)$$

$$\mathbb{D}_h = |\alpha^c \times (x_h^d)^T + B^c - Y_h^d| \otimes ((1^c + (\alpha^c)^{\odot 2})^{\odot 1/2} \times (1^d)^T) \quad (12)$$

where $(.)^T$ denotes vector transpose, $B^c \in \mathbb{R}^{N^c \times N^d}$ contains intercept values of all functions of set $g^c = \{g^{c,k}\}_{k=1:N^c}$, $Y_h^d \in \mathbb{R}^{N^c \times N^d}$ contains y Cartesian coordinates of all endpoints in set $p_h^d = \{p_h^{d,l}\}_{l=1:N^d}$, and $1^u = [1, 1, \dots, 1]^T \in \mathbb{R}^{N^u \times 1}$ is an all-ones vector. We provide in what follows the details for getting α^c , B^c , and Y_h^d . We establish α^c by indexing vector α^a using vector $I_{b,a}$, which produces vector α^b . We index the latter using vector $I_{c,b}$, producing thus desired slopes α^c . We already established both vectors $I_{b,a}$ and $I_{c,b}$ in Section 2.2.2. We show elements of B^c in equation 13 and compute them by calculating vector β^c according to equation 14 and broadcasting the result to N^d columns, as shown in equation 15. We show elements of matrix Y_h^d in equation 16 and compute them using equation 17.

$$B^c = \begin{bmatrix} \beta^{c,1} & \beta^{c,1} & \dots & \beta^{c,1} \\ \beta^{c,2} & \beta^{c,2} & \dots & \beta^{c,2} \\ \vdots & \vdots & \ddots & \vdots \\ \beta^{c,N^c} & \beta^{c,N^c} & \dots & \beta^{c,N^c} \end{bmatrix} \in \mathbb{R}^{N^c \times N^d} \quad (13)$$

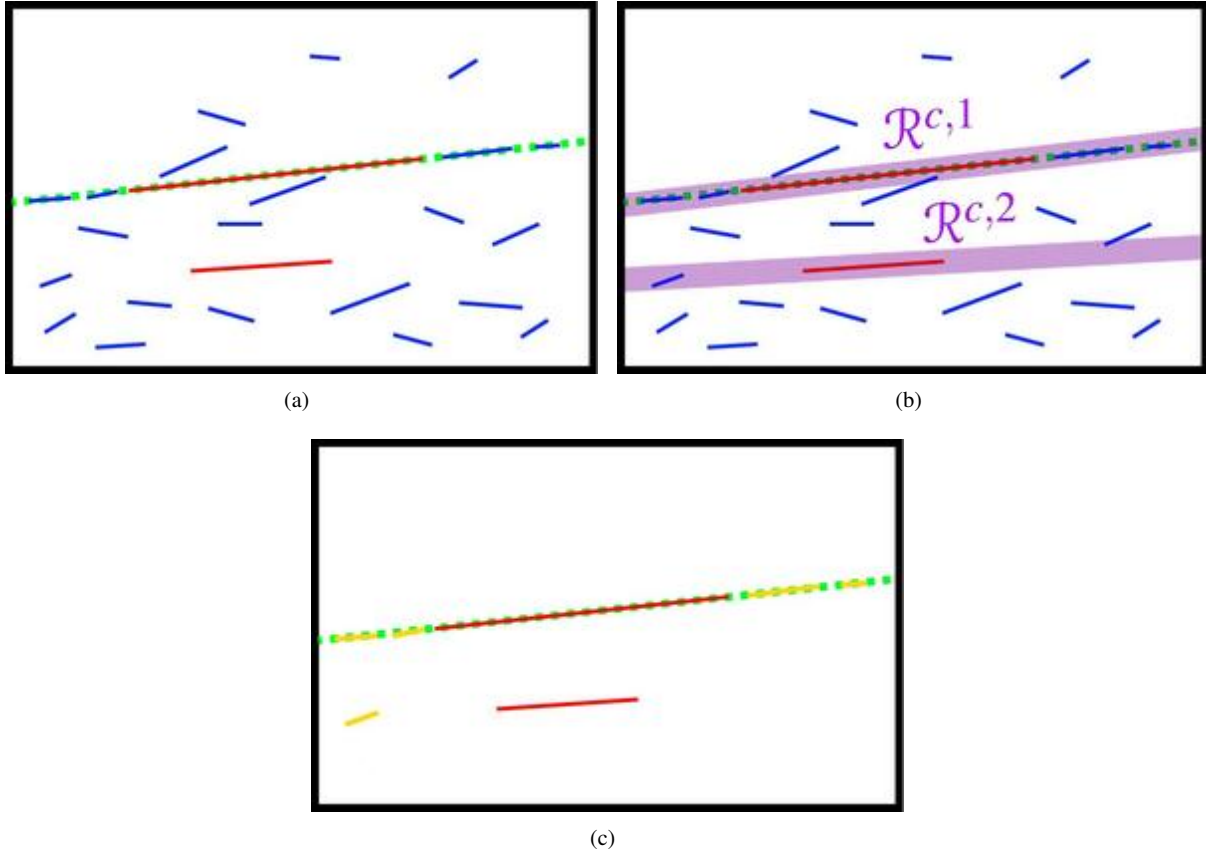


Fig. 4: A synthetic example showing the assumption made in the region of interest filter and its usage; the green dotted line is the horizon line; (a) segments of set S^c (in red) and S^d (in blue); (b) the filtering regions $\mathcal{R}^{c,1}$ and $\mathcal{R}^{c,2}$ (in pink) encompassing the two segments of set S^c ; (c) segments of set S^d that survived the two filtering regions (in yellow)

$$\beta^c = [\beta^{c,1}, \beta^{c,2}, \dots, \beta^{c,N^c}]^T \in \mathbb{R}^{N^c \times 1} \quad (14)$$

$$= y_h^c - (\alpha^c \odot x_h^c)$$

$$B^c = \beta^c \times (1^d)^T \quad (15)$$

$$Y_h^d = \begin{bmatrix} y_h^{d,1} & y_h^{d,2} & \dots & y_h^{d,N^d} \\ y_h^{d,1} & y_h^{d,2} & \dots & y_h^{d,N^d} \\ \vdots & \vdots & \ddots & \vdots \\ y_h^{d,1} & y_h^{d,2} & \dots & y_h^{d,N^d} \end{bmatrix} \in \mathbb{R}^{N^c \times N^d} \quad (16)$$

$$Y_h^d = 1^c \times (y_h^d)^T \in \mathbb{R}^{N^c \times N^d} \quad (17)$$

To exploit the distances in matrix \mathbb{D}_h , we define Q_h as in equation 18 and compute it using equation 19:

$$Q_h = \begin{bmatrix} q_h^{1,1} & q_h^{1,2} & \dots & q_h^{1,N^d} \\ q_h^{2,1} & q_h^{2,2} & \dots & q_h^{2,N^d} \\ \vdots & \vdots & \ddots & \vdots \\ q_h^{N^c,1} & q_h^{N^c,2} & \dots & q_h^{N^c,N^d} \end{bmatrix} = (q_h^{k,l}) \in \mathbb{R}^{N^c \times N^d} \quad (18)$$

$$Q_h = \mathbb{D}_h \leq T_{roi} \in \mathbb{R}^{N^c \times N^d}; \forall h \in \{s, e\} \quad (19)$$

where $q_h^{k,l}$ is a Boolean scalar whose truth indicates that end-point $p_h^{d,l} \in \mathcal{R}^{c,k}$ and $T_{roi} \in \mathbb{R}^{N^c \times N^d}$ is a matrix whose all elements are equal to t_{roi} (see equation 8). The comparison performed in equation 19 is equivalent to that of equation 8. We further process matrix Q_h using equation 20:

$$q^d = \downarrow (Q_s \tilde{\wedge} Q_e) \in \mathbb{R}^{1 \times N^d} \quad (20)$$

$$= [q^{d,1}, q^{d,2}, \dots, q^{d,N^d}]$$

where $\downarrow(\cdot)$ operator computes the logical *or* along the vertical axis of matrix Q_h ⁸, \wedge computes the element-wise logical *and*, and $q^{d,l}$ is a logical Boolean whose truth indicates that segment $S^{d,l}$ is encompassed by at least one region of interest $\mathcal{R}^{c,k}$. We note that the *and* operator used in equation 20 reflects the *and* operator in equations 7 and 8, whereas the *vertical or* operator in equation 20 reflects the \exists operator in equations 7 and 8. Thus, equation 8, equivalent to equation 7, becomes equivalent to equation 21. Subsequently, we create vector $I_{e,d}$ to contain indices where elements of vector q^d (see equation 20) are true Booleans. Finally, we establish set S^e by indexing S^d using $I_{e,d}$. We compute the final filtered set of segments output by the ROIF (stage 3 in Fig. 2) using equation 22. Fig. 3(b) and 3(f) show an example of the original set of segments S^a and the corresponding filtered set S^f , respectively.

$$S^{d,l} \in S^e \text{ if } q^{d,l} = 1 \quad (21)$$

$$S^f = S^c \cup S^e \quad (22)$$

2.4 Segments to Edge Pixels (STEP)

To get filtered edge points, we must find the coordinates of all pixels along each segment in set S^f . The number of pixels to locate for each segment $S^{f,n}$ is equal to its length $L^{f,n}$. Thus, we represent the coordinates of pixels along segment $S^{f,n}$ as in equation 23 and compute them using equation 24:

$$\begin{aligned} x^n &= [x^{n,1}, x^{n,2}, \dots, x^{n,L^{f,n}}]^T \in \mathbb{R}^{L^{f,n} \times 1} \\ y^n &= [y^{n,1}, y^{n,2}, \dots, y^{n,L^{f,n}}]^T \in \mathbb{R}^{L^{f,n} \times 1} \end{aligned} \quad (23)$$

$$\begin{aligned} x^n &= \frac{x_e^{f,n} - x_s^{f,n}}{L^{f,n} - 1} \odot z^n + x_s^{f,n} \\ y^n &= \frac{y_e^{f,n} - y_s^{f,n}}{L^{f,n} - 1} \odot z^n + y_s^{f,n} \end{aligned} \quad (24)$$

where $z^n = [0, 1, 2, \dots, L^{f,n} - 1]^T \in \mathbb{R}^{L^{f,n} \times 1}$. Because detected segments do not have the same length, we cannot further vectorize equation 24 as we did with previous equations. Therefore, we iterate over all segments of S^f . At each iteration, we compute equation 24 and append the result as expressed in equation 25:

$$\begin{aligned} x^{out} &:= x^{out} \frown x^n; \forall n \in \{1, 2, \dots, N^f - 1, N^f\} \\ y^{out} &:= y^{out} \frown y^n; \forall n \in \{1, 2, \dots, N^f - 1, N^f\} \end{aligned} \quad (25)$$

⁸ In other words, \downarrow performs the logical *or* operation on elements of each column

where $:=$ represents value assignment, \frown denotes vector appending, and x^{out} and y^{out} are vectors that would contain Cartesian coordinates of pixels along all segments in set S^f . Both x^{out} and y^{out} are initialized to an empty vector at the first iteration. Although this process is not fully vectorized, the effect on real-time performance is insignificant as the portion of survived segments in S^f is tiny compared to other sets. We will see in Section 4.4 that the execution speed achieved is satisfying.

Next, we use vectors x^{out} and y^{out} to establish an edge map image $E'(x, y)$ (see stage 4 in Fig. 2) corresponding to the downsampled image I'_{red} . Fitting the horizon line on E' works well but establishing horizon parameters corresponding to the original frame size requires scaling up the horizon position Y' corresponding to E' : $Y = Y' \times \frac{1}{\kappa}$. This affects the detected line because we amplify the error corresponding to Y' by $\frac{1}{\kappa}$. Scaling up parameters of the horizon is necessary not only for comparison with Ground Truth (GT) position Y^{GT} but also for subsequent applications. For instance, the computation of transformation matrices involved in stabilizing original video frames is directly related to horizon parameters $\{Y, \phi\}$ [12–14]. Therefore, we infer the horizon line by relocating edge points of E' on an edge map E (see stage 4 in Fig. 2) with the original frame size. Thus, we significantly mitigate the amplified error and leverage image downsizing. We compute E by upsampling E' to the original frame size using a bilinear interpolation method, which outputs grayscale image E'' with thicker edges. We shrink the thickness of the latter to one pixel using the nonmaximum suppression method, followed by a single-thresholding of E'' with $E_{th} = 254$. This outputs image E , which contains relocated edge points. Figure 5 shows the edge map E corresponding to challenging conditions, such as weak horizon edges, coastal boundaries, and highly textured regions induced by sea waves, glints, and clouds; the large number of segments S^a in Fig. 5(b) indicates the high amount of noise; Fig. 5(c) demonstrates that the high image clutter is significantly suppressed while favoring horizon edges to form the most prominent line. Edges of the horizon line corresponding to the right image of Fig. 5(a) are dramatically affected by the smooth color transition between the sea and sky. However, the corresponding edge map in Fig. 5(c) demonstrates that the filtering stages kept enough horizon edges for accurate detection. This will be further demonstrated qualitatively and quantitatively in Section 4.4.

2.5 Horizon line inference

We infer the horizon line in three major steps (see stage 5 in Fig. 2). The Outlier Handler Module (OHM) verifies that the global maximum of the accumulated Hough space, denoted as $\{Y^{Jc}, \phi^{Jc}\}$, is not an outlier. We define outlier lines as false-positive horizons persisting over a very brief

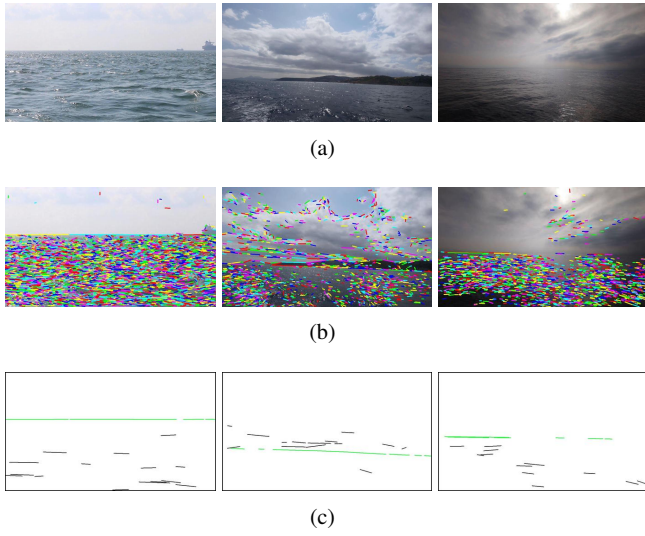


Fig. 5: Illustration of the output edge map E ; (a) original images; (b) all detected line segments; (c) the output edge map E . For visualization convenience, the binary edges in (c) are dilated and inverted, and the horizon edges are colored in green.

period. This issue occurs on other algorithms we tested in this paper as well. In our case, outlier lines appear primarily due to noisy segments of the sea region that occasionally line up to survive the ROIF. The OHM considers $\{Y^{\mathcal{J}^c}, \phi^{\mathcal{J}^c}\}$ as an outlier line if the condition in equation 26 is satisfied:

$$(|Y^{\mathcal{J}^c} - Y^{prv}| > \Delta Y^{th}) \vee (|\phi^{\mathcal{J}^c} - \phi^{prv}| > \Delta \phi^{th}) = 1 \quad (26)$$

where \vee is the logical *or*, $\{Y^{prv}, \phi^{prv}\}$ are parameters of the most recent horizon line, and $\{\Delta Y^{th}, \Delta \phi^{th}\}$ are scalar thresholds. If $\{Y^{\mathcal{J}^c}, \phi^{\mathcal{J}^c}\}$ is not an outlier, we consider it a coarse estimation of the horizon line: $\{Y^{\mathcal{J}^c}, \phi^{\mathcal{J}^c}\} = \{Y^{crs}, \phi^{crs}\}$. Otherwise, if $\{Y^{\mathcal{J}^c}, \phi^{\mathcal{J}^c}\}$ is an outlier, the OHM will consider that the coarse horizon line $\{Y^{crs}, \phi^{crs}\}$ is one of the longest M Hough lines satisfying equation 26. If multiple lines satisfy such a condition, we select the line corresponding to the minimum value $|Y^{\mathcal{J}^c} - Y^{prv}|$. To refine the coarse line $\{Y^{crs}, \phi^{crs}\}$, we follow Jeong et al. [32] by applying the least-squares fitting algorithm on *inlier edge points*, i.e., edge points that voted on $\{Y^{crs}, \phi^{crs}\}$.

Ettinger et al. [36] pointed out that using previous detections of the horizon line to infer the horizon may get the algorithm into a failure state; concretely, if the algorithm detects a faulty line, it will incorrectly update the parameters of the most recent horizon line $\{Y^{prv}, \phi^{prv}\}$. Therefore, the outlier condition in equation 26 becomes useless if the difference between that faulty line and the true horizon exceeds a certain threshold. When this issue occurs, the faulty horizon is unlikely to be persistently detected on subsequent frames, either due to the changing sea noise or the linear property of the horizon that would compete with that faulty line. Thus, the outlier condition triggers on a signifi-

cant number of consecutive frames. The OHM counts this number, denoted as N_{outs} , and compares it to a threshold N_{outs}^{th} . If $N_{outs} > N_{outs}^{th}$, the OHM considers that the algorithm is in a failure state. To get the algorithm out of this state, the OHM avoids finding a substitute line and directly refines the longest Hough line $\{Y^{\mathcal{J}^c}, \phi^{\mathcal{J}^c}\}$ using the least-squares fitting. This process quickly converges to correctly updating the parameters $\{Y^{prv}, \phi^{prv}\}$. The reader may question the usefulness of the OHM as it seems to create the same problem that it solves. From one hand, the OHM is supposed to correct outlier horizons, which are fundamentally incorrect detections. On the one hand, the OHM may get the algorithm into a failure state that may lead to incorrect detections again. The OHM is effective because the incorrect detections caused by failure states are negligible compared to the incorrect detections corresponding to outlier lines. We quantitatively justify the effectiveness of the OHM in Section 4.5 by ablating it from the overall algorithm.

3 Proposing a new sea horizon dataset

An ideal sea horizon dataset should contain carefully annotated video clips depicting a comprehensive set of maritime conditions. The horizon annotation is necessary for the quantitative evaluation of a given algorithm. The annotation files provide GT values of the horizon position Y and tilt ϕ (see Figure 6).

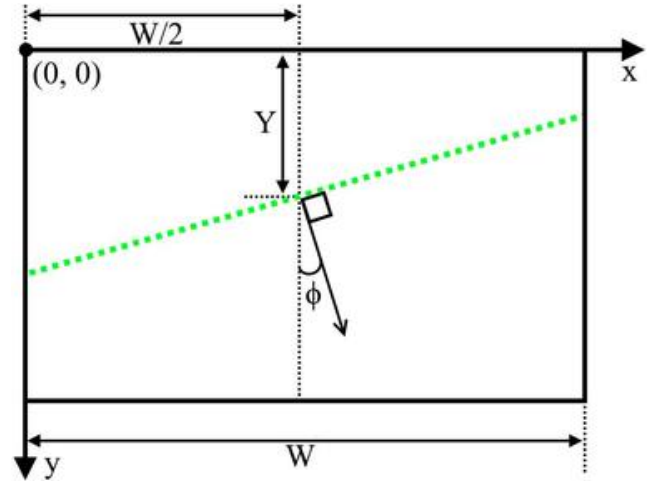


Fig. 6: Position Y and tilt ϕ of the horizon

There are several maritime datasets such as [14, 38, 44], but they lack high-resolution images [14, 38], horizon line annotations [38], diversity of conditions [14], temporal information (i.e., consecutive video frames) [38, 44], or low altitude images reflecting the conditions faced by surface marine vehicles [44]. As far as we know, the SMD [1] is

the largest and most diverse public dataset without the previous drawbacks. Student volunteers⁹ annotated the SMD, which was collected using two setups: the onshore and on-board setup¹⁰.

The SMD lacks important maritime scenes, which have the potential to break assumptions of state-of-the-art algorithms. To fulfill such a gap, we introduce the Moroccan Maritime Dataset (MMD), which contains 18 high-resolution visible-range videos captured onboard a surface vehicle around Morocco’s Mediterranean sea. We carefully annotated the MMD using a custom software that we developed in Python and Tkinter [45] (see Fig. 7). We verified the accuracy of each frame annotation. To suit both Python and Matlab users, we share the horizon annotations as *.npy* and *.mat* files with a description file (see *Description of the dataset.pdf* in the provided link). We highlight in Table 1 major maritime challenges existing in the MMD and SMD; our dataset contains nine maritime scenarios that do not exist in the SMD. Figure 8 shows one sample frame from each video clip of the proposed MMD. Table 2 shows video properties and statistical details of the datasets we used in Section 4.4.

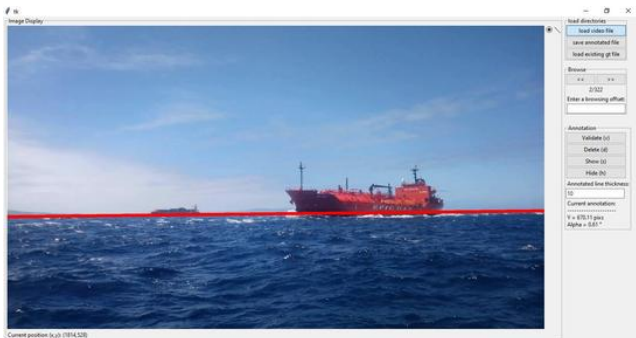


Fig. 7: A snap of the GUI of our annotation software after annotating the horizon line (in red)

4 Experiments

4.1 Benchmarked algorithms

4.1.1 Implementations and important considerations

We compare our algorithm with an extensive set of six state-of-the-art algorithms: [6, 7, 9, 22, 30, 32]. We used our

⁹ We had to correct several incorrect annotations of the SMD before using it in the experiments.

¹⁰ *Onshore* means that the camera is mounted on a stationary shore platform, whereas *onboard* means that the camera is mounted on a offshore non-stationary platform (e.g., buoy or a ship)

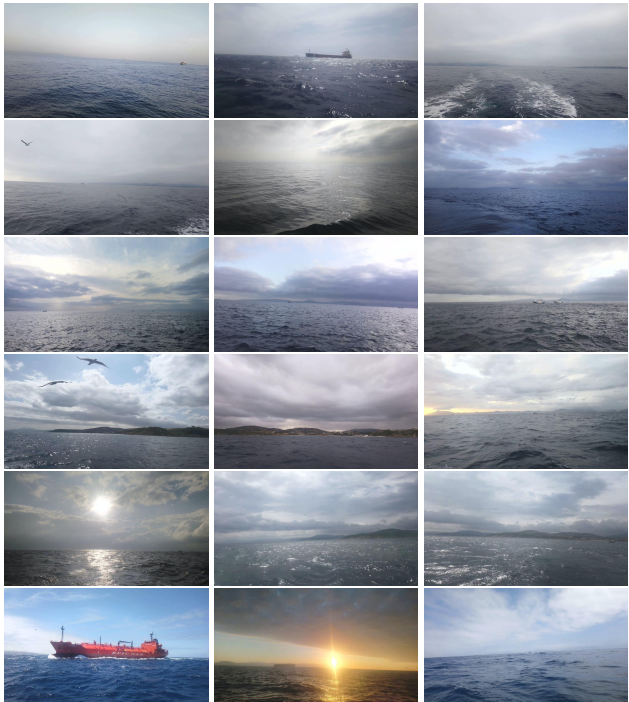


Fig. 8: One sample frame from each video clip of the MMD

own implementation for [6, 9, 22, 32] since we could not access the source code of its original authors. We managed to get the source code of the original authors for the remaining two algorithms [7, 30].

While the algorithm proposed in [9] was not originally intended for maritime images, we included it in our experimental comparison due to its reported capability to extract weak horizon edges from scenes captured in various wild environments. This algorithm employs dynamic programming (DP) to infer the non-linear skyline separating the sky and mountain. This DP relies on rules and preferences that are not applicable to the linear horizon of maritime images. To ensure a fair comparison, we substituted the DP inference with the most accurate horizon line fitting method available in the literature, as proposed by Jeong et al [32, 33]. Regarding the other algorithms developed for maritime images, we used the same algorithm parameters provided in the original implementations or specified in the published papers.

4.1.2 Parameters of our algorithm

For generalization purposes, we did not perform any quantitative optimization study to fix the parameters of our algorithm. Instead, we selected their values based on our knowledge of their effect and our visual analysis of intermediate results (i.e., the output of different stages and modules) on a representative set of images. We show in Table 3 all parameter values we used in our algorithm to produce the experimental results. We note that we kept these exact param-

Table 1: Diversity comparison between the Moroccan Maritime Dataset with the Singapore Maritime Dataset. \mathcal{S} , \mathcal{M} , and \mathcal{B} mean that the condition exists in (i) the SMD only, (ii) the MMD only, and (iii) both SMD and MMD, respectively.

Sea variables					Sky variables						Horizon visibility			Classes above the horizon			Time of the day		
1. Small waves	2. Scattered sun glints	3. Grouped sun glints	4. Smooth surface	5. Wakes	6. Clear	7. Small clouds	8. Linear-edged clouds	9. Smooth overcast	10. Textured overcast	11. Visible Sun	12. Medium contrast	13. Weak horizon edges	14. Partial ship occlusion	15. Sky	16. Coast	17. Sky and coast	18. Sunrise and sunset	19. Daytime	20. After sunset
\mathcal{B}	\mathcal{B}	\mathcal{M}	\mathcal{M}	\mathcal{B}	\mathcal{B}	\mathcal{B}	\mathcal{M}	\mathcal{B}	\mathcal{M}	\mathcal{M}	\mathcal{B}	\mathcal{M}	\mathcal{B}	\mathcal{B}	\mathcal{M}	\mathcal{M}	\mathcal{M}	\mathcal{B}	\mathcal{S}

Table 2: Video properties and statistical details datasets

	SMD		MMD
	Onboard	Onshore	
Number of video files	37	11	18
Total number of frames	2813	17222	6090
Frames per video	$\in [255, 299]$	$\in [206, 995]$	$\in [273, 405]$
Size of frames (width \times height)	1920×1080	1920×1080	1920×1080
FPS	30.0	30.0	29.605
Channels	RGB	RGB	RGB

eters on all three datasets (SMD-Onshore, SMD-Onboard, and MMD).

Table 3: Values of our method’s parameters

Stages	Parameter values
Stage 1	Downsampling factor $\kappa = 0.6$; LSD parameters: Sobel kernel = 3×3 , Canny’s upper and lower thresholds: 25 and 45.
Stage 2	$\alpha_{th} = 0.57, N^c = 15; N^d = 200$
Stage 3	$t_{roi} = 2$ pixels
Stage 4	Parameterless
Stage 5	Hough space $H(\rho, \theta)$: $\Delta\rho = 2$ pixels, $\Delta\theta = 1^\circ$; OHM: $\Delta Y^{th} = 2.6\% \times \text{Image Height} = 50$ pixels, $\Delta\phi^{th} = 2^\circ, M = 2, N_{outs}^{th} = 5$.

4.2 Comparison metrics

We parameterize the detected horizon line using the position Y and tilt ϕ we previously exposed in Fig. 6. We quantify the detection error by computing $Y^\varepsilon = |Y - Y^{GT}|$ and

$\phi^\varepsilon = |\phi - \phi^{GT}|$, where the pair $\{Y^{GT}, \phi^{GT}\}$ corresponds to parameters of the GT (Ground Truth) horizon. Eventually, we use errors computed for each dataset to extract the following six statistical metrics: μ , σ , Q25, Q50, Q75, and Q95, where μ and σ correspond to the mean and standard deviation, respectively, and QP is the P -th percentile. To quantify the real-time performance, we measure the mean processing time of all algorithms on each dataset. We also report the visual results of each algorithm on six representative maritime images.

4.3 Hardware and software

The original authors of [7, 30] provided their implementations on MATLAB. We implemented all the remaining algorithms [6, 9, 22, 32], including ours, on Python 3.8, utilizing the packages *Numpy* and *OpenCV* [46, 47]. We ran each compared algorithm, one at a time, on a computer with 8GB of RAM and one Intel® Core™ i5-6300U CPU @ 2.40GHz, ensuring a fair comparison by halting all tasks that may use the computer’s CPU during each algorithm’s execution.

4.4 Experimental results and discussion

We quantitatively compare the horizon position error Y^ε and tilt error ϕ^ε of all algorithms in Tables 4, 5, and 6. Tables 4 and 5 show that our algorithm and Jeong et al.’s method [32] perform significantly better on the SMD. Table 4 shows that our method performed the best in 9 metrics (out of 12), while Jeong et al.’s method [32] scored the best on the remaining three metrics. We expected this particular result for [32] because its multi-scale median filter is highly effective against various sea clutter when the horizon has a prominent length and edges, which is the case in most SMD-onboard videos. Compared to Table 4, Table 5 shows an accuracy decline for [6, 7, 32] and our method. Our decline is likely because the horizon in SMD-onshore videos is relatively shorter due to ship occlusion and mixed with

additional clutter, such as linear wakes and ships' contours. This interpretation may apply, at least to some extent, to the other methods. Nevertheless, Table 5 shows that our method performs remarkably better in 11 (out of 12) metrics while scoring a very competitive value on the remaining metric σ .

Table 6 shows that our algorithm achieves the lowest error on all 12 metrics when tested on the MMD, and the error gap between our method and all six state-of-the-art algorithms is remarkably high. As the MMD dataset introduces various new conditions, including images with weak horizon edges, the final result strongly indicates our method's significant robustness against such edges. We support this claim with qualitative results as well: Figures 9 to 16 visually compare the algorithms' output on six image samples. By examining the first row of images Fig. 10 with state-of-the-art, we can see that our algorithm reliably and accurately handles weak horizon edges. Moreover, the second row of Fig. 10 shows accurate results in other challenging clutter, including strong and connected coastal boundaries, sun glints, textured clouds, and ships' contours. While the horizon in coastal images can often appear as a prominent and strong line (e.g., the middle image of the second row in Fig. 9), several state-of-the-art algorithms failed mainly due to the persistence of strong sky-coast edges after filtering. We observed that these edges have little impact on our algorithm because their gradient angles are unstable, limiting the length of corresponding line segments and increasing their suppression rate in stage 2 (see Fig. 2).

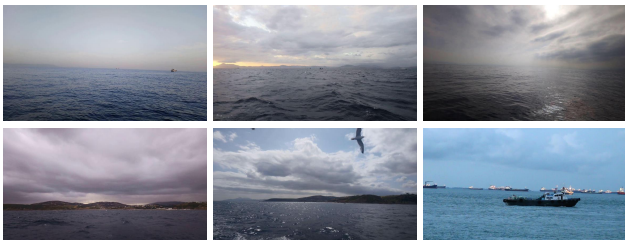


Fig. 9: Original images

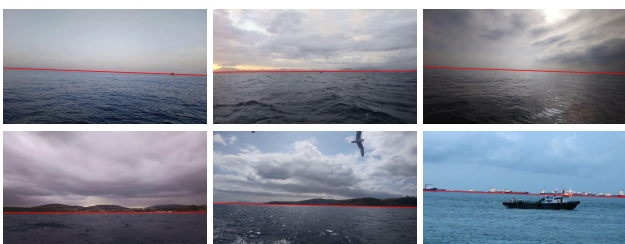


Fig. 10: Results on samples of Fig. 9 (Ours)



Fig. 11: Results on samples of Fig. 9 (Li et al. [6])

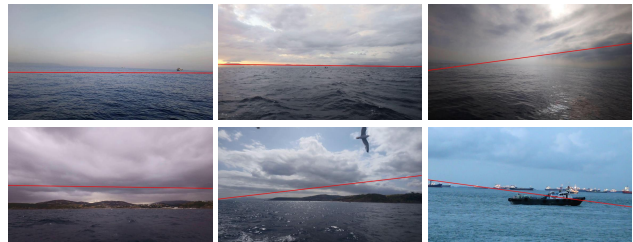


Fig. 12: Results on samples of Fig. 9 (Liang and Liang [7])

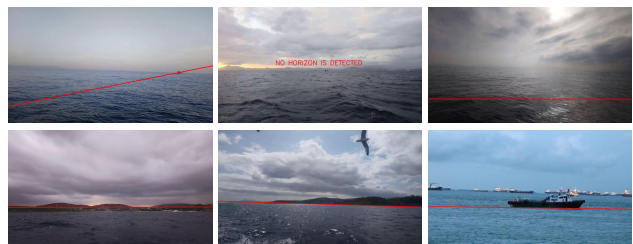


Fig. 13: Results on samples of Fig. 9 (Jeong et al. [32])

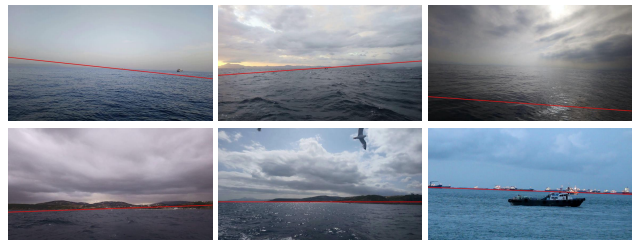


Fig. 14: Results on samples of Fig. 9 (Prasad et al. [30])

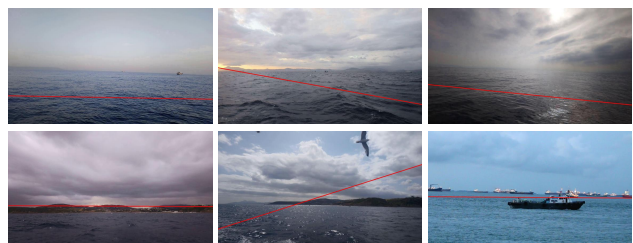


Fig. 15: Results on samples of Fig. 9 (Gershikov et al. [22])

Table 7 shows the execution time of all methods on each dataset. The fastest algorithm is [22], while the slowest is [30]. From the perspective of computational speed, our al-

Table 4: Quantitative results on *onboard* videos of the Singapore Maritime Dataset

	$Y^\epsilon = Y - Y^{GT} $ in pixels						$\phi^\epsilon = \phi - \phi^{GT} $ in degrees					
	μ	σ	Q25	Q50	Q75	Q95	μ	σ	Q25	Q50	Q75	Q95
Ours	1.95	1.59	0.84	1.71	2.71	4.57	0.16	0.13	0.060	0.13	0.23	0.41
Li [6]	34.64	73.96	14.35	22.72	30.84	71.49	0.85	1.46	0.37	0.64	1	1.70
Liang [7]	17.77	46.93	0.90	2.13	7.65	93.43	4.71	3.38	2.53	4.27	6.28	10.09
Jeong [32]	3.84	33.09	0.68	1.43	2.44	4.86	0.26	1.61	0.065	0.144	0.25	0.50
Prasad [30]	210.50	212.81	2.51	198.68	386.00	564.98	2.65	2.40	0.84	2.00	3.74	7.50
Gershikov [22]	301.44	145.02	186.67	334.50	410.28	510.67	6.55	6.85	1.60	3.84	9.17	22.10
Lie [9]	210.67	129.62	115.89	214.81	297.31	429.40	2.26	1.95	0.71	1.94	3.26	6.00

Table 5: Quantitative results on *onshore* videos of the Singapore Maritime Dataset

	$Y^\epsilon = Y - Y^{GT} $ in pixels						$\phi^\epsilon = \phi - \phi^{GT} $ in degrees					
	μ	σ	Q25	Q50	Q75	Q95	μ	σ	Q25	Q50	Q75	Q95
Ours	5.66	11.20	1.20	2.56	5.15	22.62	0.22	0.25	0.05	0.14	0.33	0.66
Li [6]	50.49	97.13	7.24	17.73	48.14	246.26	1.07	2.23	0.17	0.39	1.13	4.26
Liang [7]	31.50	49.19	2.50	17.65	33.13	151.97	3.40	4.13	0.48	1.72	4.85	12.81
Jeong [32]	7.86	12.56	1.68	3.61	8.60	29.62	0.28	0.22	0.12	0.24	0.37	0.72
Prasad [30]	12.83	37.99	1.93	3.60	7.49	43.18	2.16	2.29	0.30	1.86	3.75	6.33
Gershikov [22]	119.03	93.29	30.62	99.83	185.74	284.41	5.09	5.37	1.19	2.89	7.20	17.20
Lie [9]	199.23	147.25	101.05	186.07	275.21	484.29	1.30	1.86	0.16	0.41	1.76	5.21

Table 6: Quantitative results on the Moroccan Maritime Dataset

	$Y^\epsilon = Y - Y^{GT} $ in pixels						$\phi^\epsilon = \phi - \phi^{GT} $ in degrees					
	μ	σ	Q25	Q50	Q75	Q95	μ	σ	Q25	Q50	Q75	Q95
Ours	4.35	3.70	2.16	3.72	5.70	9.21	0.23	0.26	0.07	0.15	0.32	0.63
Li [6]	50.32	81.28	8.83	19.21	52.85	245.61	1.63	2.66	0.37	0.80	1.47	7.20
Liang [7]	123.57	189.78	10.31	55.66	143.41	749.97	4.94	4.87	1.71	3.74	6.66	13.26
Jeong [32]	150.09	3785.03	2.67	5.47	28.03	225.98	1.81	7.42	0.12	0.33	0.66	6.90
Prasad [30]	99.62	143.73	3.54	8.00	197.49	396.20	4.89	4.37	1.72	3.78	7.01	13.19
Gershikov [22]	148.15	100.10	63.37	143.38	205.94	331.05	7.14	5.90	2.37	5.78	10.26	19.61
Lie [9]	118.43	108.17	16.46	95.17	197.25	313.10	2.15	2.53	0.36	1.23	3.00	7.68

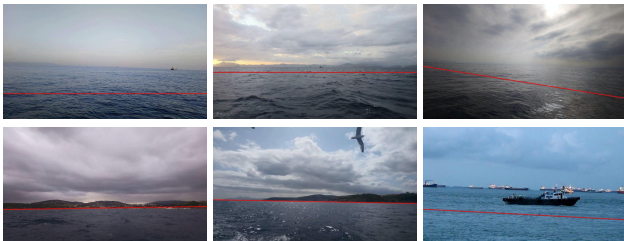


Fig. 16: Results on samples of Fig. 9 (Lie et al. [9])

gorithm is not the fastest as it takes, on average, 1.78 times longer than the fastest algorithm. However, on the onboard

and onshore datasets, we maintain a very competitive speed with the next fastest methods [7, 9, 32]. On the MMD, our algorithm is the second fastest after [22]. This difference in speed compared to the other two datasets is due to the lower contrast of images, which means the LSD grows fewer line segments, hence less processing time.

The computational speed is an essential factor, but the real-time performance also involves accuracy and robustness. While our method is 1.78 slower than the fastest method [22], the latter has for instance, a mean positional error Y^ϵ that's at least 21 times higher than ours. While we maintain a highly competitive speed against the most accu-

rate methods, our accuracy surpasses both the fastest [7, 9, 22, 32] and the slowest algorithms [6, 30] with a significant margin, which indicates our superior real-time performance.

Table 8 demonstrates the efficiency of our proposed filter in stages 2, 3, and 4, with a computational load of less than 1.8% of the overall process, providing quantitative evidence of our technique’s effectiveness in addressing computational demands. Notably, the computational time of the employed LSD [42] is at least 62%, and the literature on LSD includes superior algorithms. For instance, the LSD proposed by Akinlar and Topal [43] is 11 times faster than the LSD [42] we used in this paper. Thus, we can significantly boost the computational speed of our method while enhancing its accuracy just by using an alternative LSD in stage 1 (Figure 2).

Table 7: Mean computational time per frame on the SMD (Onboard and Onshore) and MMD (in milliseconds)

	Onboard	Onshore	MMD
Ours	107.6	101.4	70.3
Li [6]	486.5	426.0	418.8
Liang [7]	73.7	79.4	74.6
Jeong [32]	90.6	95.7	85.4
Prasad [30]	1979.4	1946.1	1932.6
Gershikov [22]	50.6	53.0	52.7
Lie [9]	141.8	101.4	111.5

Table 8: The computational time ratio of components of our algorithm from the mean time shown in the first row of Table 7

	Onboard	Onshore	MMD
LSD [42]	75.38%	72.37%	62.96%
Stage 1	80.52%	78.5%	71.66%
Stage 2, 3, and 4	0.8%	1.52%	1.71%
Stage 5	18.68%	19.94%	26.48%

4.5 Ablation study

In this section, we ablate the key components of our algorithm. The results presented in Table 9 demonstrate that the original algorithm, incorporating both the ROIF and OHM, achieves the highest accuracy with the lowest errors in 9 out of 12 metrics. Removing either the ROIF or OHM component results in decreased accuracy, confirming the experimental validation of both components.

Table 9: The quantitative results obtained after removing different algorithm components; the results are obtained on the combination of the SMD and MMD, which amount to 26,125 frames

	$Y^e = Y - Y^{GT} $ in pixels					
	μ	σ	Q25	Q50	Q75	Q95
Original	4.96	9.36	1.30	2.69	4.98	20.28
Without ROIF	4.93	7.46	1.37	2.74	5.18	19.82
Without OHM	7.51	28.12	1.31	2.73	5.12	22.15
	$\phi^e = \phi - \phi^{GT} $ in degrees					
	μ	σ	Q25	Q50	Q75	Q95
Original	0.22	0.23	0.054	0.14	0.31	0.64
Without ROIF	0.23	0.25	0.055	0.15	0.33	0.67
Without OHM	0.23	0.30	0.055	0.15	0.32	0.66

4.6 Limitation of our method

We illustrate the limitation of the proposed algorithm in Fig. 17, which occurs due to occasional scenarios depicting faulty lines with stable gradient orientations. The limitation example in Fig. 17(b) is more difficult because the bulk does not only induce a faulty line but shrinks the length property of the horizon as well. This issue occurs on all algorithms we tested. In our case, however, such an issue is mitigated thanks to the OHM; in Fig. 17(c), the positional error gap Y^e between the true horizon (in yellow) and the faulty line (in pink) induced by ship edges is larger than the other two errors. This gap allowed the OHM to detect and replace the incorrect horizon line with the correct one.

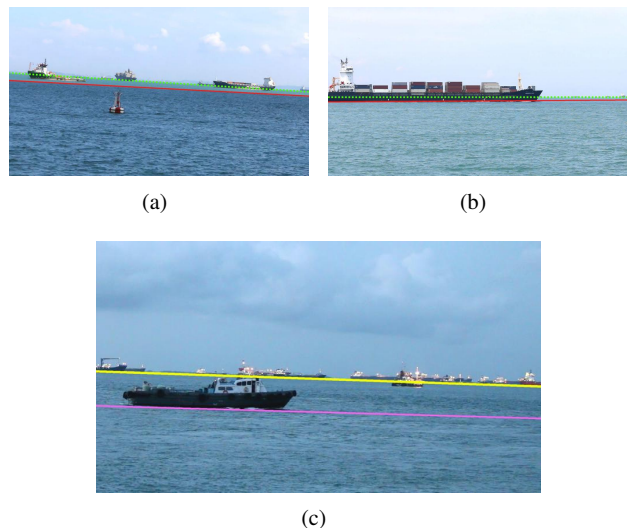


Fig. 17: Limitation examples: in (a) and (b), the green dotted line is the ground truth horizon, and the red line is the incorrect detection of our method; in (c), the incorrect detection (in pink) is successfully replaced with the correct line (in yellow) thanks to the OHM.

5 Conclusions and future work

The sea horizon is a critical element in maritime video processing, and detecting it under a variety of conditions, especially when the horizon edge response is weak, is a challenging task. In this paper, we proposed a novel method for horizon line detection that outperforms six state-of-the-art methods under weak edge response conditions, while also achieving better results in other scenarios. Our method's key improvement is its filtering approach, which preserves weak horizon edges while exploiting the properties of line segments detected with a low edge threshold. We also addressed the computational constraint by proposing a vectorized implementation for efficient CPU execution and by accurately projecting the detected horizon from the downsized image to the original size. In addition, we have made a new maritime dataset (the MMD) publicly available, which is enriched with images from various sea conditions. We expect our algorithm's modular design to be valuable for other researchers, as it enables them to integrate functional stages, like our robust outlier handler module, into their own work. Our method is limited by noisy lines with stable gradient orientation or heavily occluded horizons. We have partially mitigated this limitation by using temporal information, but we believe that an efficient convolutional neural network approach to classify edge pixels output by our filter could address this limitation.

Data and material availability

The material used to produce the experimental results of this study is available upon a reasonable request to the authors. Source code and dataset files are available at: https://drive.google.com/drive/folders/1bh2MdvU_NV8pG7Ypo6Rdd86BThTjqj5U?usp=sharing

Acknowledgments

We would like to express our gratitude to Sailor, Mr. Mustapha Tayebioui, for his invaluable assistance in collecting the Moroccan Maritime Dataset.

Compliance with Ethical Standards

Disclosure of potential conflicts of interest On behalf of all authors, the corresponding author states that there is no conflict of interest.

Research involving human participants and/or animals

This article does not contain any studies with human participants or animals performed by any of the authors.

Funding No funding was received for conducting this work.

References

1. Prasad, D. K., Rajan, D., Rachmawati, L., Rajabally, E. & Quek, C. Video Processing From Electro-Optical Sensors for Object Detection and Tracking in a Maritime Environment: A Survey. *IEEE Transactions on Intelligent Transportation Systems* **18**, 1993–2016. ISSN: 1558-0016. <https://doi.org/10.1109/TITS.2016.2634580> (2017).
2. Petković, M., Vujović, I. & Kuzmanić, I. An Overview on Horizon Detection Methods in Maritime Video Surveillance. *Transactions on Maritime Science* **9**, 106–112. <https://doi.org/10.7225/toms.v09.n01.010> (2020).
3. Zardoua, Y., Astito, A. & Boulaala, M. A survey on horizon detection algorithms for maritime video surveillance: advances and future techniques. *The Visual Computer* **39**, 197–217. ISSN: 1432-2315. <https://doi.org/10.1007/s00371-021-02321-0> (2023).
4. Shao, Z., Wang, L., Wang, Z., Du, W. & Wu, W. Saliency-aware convolution neural network for ship detection in surveillance video. *IEEE Transactions on Circuits and Systems for Video Technology* **30**, 781–794 (2019).
5. Dong, L., Ma, D., Ma, D. & Xu, W. Fast infrared horizon detection algorithm based on gradient directional filtration. *J. Opt. Soc. Am. A* **37**, 1795–1805. [10.1364/JOSAA.402620](https://doi.org/10.1364/JOSAA.402620) (2020).
6. Li, F. *et al.* Sea-sky line detection using gray variation differences in the time domain for unmanned surface vehicles. *Signal, Image and Video Processing* **15**, 139–146. ISSN: 1863-1711. <https://doi.org/10.1007/s11760-020-01733-0> (2021).
7. Liang, D. & Liang, Y. Horizon Detection From Electro-Optical Sensors Under Maritime Environment. *IEEE Transactions on Instrumentation and Measurement* **69**, 45–53. ISSN: 1557-9662. <https://doi.org/10.1109/TIM.2019.2893008> (2020).
8. Yang, D. *et al.* A review of intelligent ship marine object detection based on RGB camera. *IET Image Processing* (2023).
9. Lie, W.-N., Lin, T. C.-I., Lin, T.-C. & Hung, K.-S. A robust dynamic programming algorithm to extract skyline in images for navigation. *Pattern Recognition Letters* **26**, 221–230. ISSN: 0167-8655. <https://doi.org/10.1016/j.patrec.2004.08.021> (2005).
10. Ahmad, T., Emami, E., Čadík, M. & Bebis, G. *Resource Efficient Mountainous Skyline Extraction using Shallow Learning in 2021 International Joint Conference on Neural Networks (IJCNN)* (2021), 1–9. [10.1109/IJCNN52387.2021.9533859](https://doi.org/10.1109/IJCNN52387.2021.9533859).
11. Zardoua, Y., Astito, A., Boulaala, M. & Dokkali, Y. *A Short Overview of Horizon Detection Methods Applied to Maritime Video Stabilization in Advanced Intelligent Systems for Sustainable Development (AI2SD'2020)* (eds Kacprzyk, J., Balas, V. E. & Ezziyyani, M.) (Springer International Publishing, Cham, 2022), 857–864. ISBN: 978-3-030-90639-9.
12. Schwendeman, M. & Thomson, J. A Horizon-Tracking Method for Shipboard Video Stabilization and Rectification. *Journal of Atmospheric and Oceanic Technology* **32**, 164–176. <https://doi.org/10.1175/JTECH-D-14-00047.1> (2015).
13. Cai, C., Weng, X. & Zhu, Q. Sea-skyline-based image stabilization of a buoy-mounted catadioptric omnidirectional vision system. *EURASIP Journal on Image and Video Processing* **2018**, 1. ISSN: 1687-5281. <https://doi.org/10.1186/s13640-017-0240-z> (2018).
14. Fefilat'ev, S., Goldgof, D., Shreve, M. & Lembke, C. Detection and tracking of ships in open sea with rapidly moving buoy-mounted camera system. *Ocean Engineering* **54**, 1–12. ISSN: 0951-9852. <https://doi.org/10.1016/j.oceaneng.2012.09.010> (2012).

- 0029-8018. <https://doi.org/10.1016/j.oceaneng.2012.06.028> (2012).
15. Liu, J., Li, H., Liu, J., Xie, S. & Luo, J. Real-Time Monocular Obstacle Detection Based on Horizon Line and Saliency Estimation for Unmanned Surface Vehicles. *Mobile Networks and Applications* **26**, 1372–1385. ISSN: 1572-8153. <https://doi.org/10.1007/s11036-021-01752-2> (2021).
 16. Kong, W. & Hu, T. A deep neural network method for detection and tracking ship for unmanned surface vehicle in 2019 IEEE 8th Data Driven Control and Learning Systems Conference (DDCLS) (2019), 1279–1283.
 17. Fu, J., Li, F., Zhao, J., Tong, J. & Zhang, H. Infrared Small Dim Target Detection Under Maritime Near Sea-sky Line Based on Regional-Division Local Contrast Measure. *IEEE Geoscience and Remote Sensing Letters* (2023).
 18. Gladstone, R., Moshe, Y., Barel, A. & Shenhav, E. Distance estimation for marine vehicles using a monocular video camera in 2016 24th European Signal Processing Conference (EUSIPCO) (2016), 2405–2409.
 19. Jia, B., Liu, R. & Zhu, M. Real-time obstacle detection with motion features using monocular vision. *The Visual Computer* **31**, 281–293 (2015).
 20. Polvara, R., Sharma, S., Wan, J., Manning, A. & Sutton, R. Obstacle avoidance approaches for autonomous navigation of unmanned surface vehicles. *The Journal of Navigation* **71**, 241–256 (2018).
 21. Samama, A. Innovative video analytics for maritime surveillance in 2010 International WaterSide Security Conference (2010), 1–8. <https://doi.org/10.1109/WSSC.2010.5730280>.
 22. Gershikov, E., Libe, T. & Kosolapov, S. Horizon line detection in marine images: which method to choose? *International Journal on Advances in Intelligent Systems* **6** (2013).
 23. Bao, G.-Q., Xiong, S.-S. & Zhou, Z.-Y. Vision-based horizon extraction for micro air vehicle flight control. *IEEE Transactions on Instrumentation and Measurement* **54**, 1067–1072 (2005).
 24. Zhang, H., Yin, P., Zhang, X. & Shen, X. A robust adaptive horizon recognizing algorithm based on projection. *Transactions of the Institute of Measurement and Control* **33**, 734–751. eprint: <https://doi.org/10.1177/0142331209342201>. <https://doi.org/10.1177/0142331209342201> (2011).
 25. Shen, Y., Rahman, Z., Krusienski, D. & Li, J. A Vision-Based Automatic Safe Landing-Site Detection System. *IEEE Transactions on Aerospace and Electronic Systems* **49**, 294–311. ISSN: 1557-9603. <https://doi.org/10.1109/TAES.2013.6404104> (2013).
 26. Shen, Y.-F., Krusienski, D., Li, J. & u. Rahman, Z. A Hierarchical Horizon Detection Algorithm. *IEEE Geoscience and Remote Sensing Letters* **10**, 111–114. ISSN: 1558-0571. <https://doi.org/10.1109/LGRS.2012.2194473> (2013).
 27. Lipschutz, I., Gershikov, E. & Milgrom, B. New methods for horizon line detection in infrared and visible sea images. *Int. J. Comput. Eng. Res* **3**, 1197–1215 (2013).
 28. Ohki, M., Zervakis, M. E. & Venetsanopoulos, A. N. in *Multidimensional Systems: Signal Processing and Modeling Techniques* (ed Leondes, C.) 49–88 (Academic Press, 1995). <https://www.sciencedirect.com/science/article/pii/S0090526705800386>.
 29. Romeny, B. M. H. *Front-end vision and multi-scale image analysis: multi-scale computer vision theory and applications, written in mathematica* (Springer Science & Business Media, 2008).
 30. Prasad, D. K. et al. MSCM-LiFe: Multi-scale cross modal linear feature for horizon detection in maritime images in 2016 IEEE Region 10 Conference (TENCON) (2016), 1366–1370. <https://doi.org/10.1109/TENCON.2016.7848237>.
 31. Prasad, D. K., Rajan, D., Rachmawati, L., Rajabally, E. & Quek, C. MuSCoWERT: multi-scale consistence of weighted edge Radon transform for horizon detection in maritime images. *J. Opt. Soc. Am. A* **33**, 2491–2500. <https://doi.org/10.1364/JOSAA.33.002491> (2016).
 32. Jeong, C. Y., Yang, H. S. & Moon, K. Fast horizon detection in maritime images using region-of-interest. *International Journal of Distributed Sensor Networks* **14**, 1550147718790753. eprint: <https://doi.org/10.1177/1550147718790753>. <https://doi.org/10.1177/1550147718790753> (2018).
 33. Jeong, C., Yang, H. S. & Moon, K. A novel approach for detecting the horizon using a convolutional neural network and multi-scale edge detection. *Multidimensional Systems and Signal Processing* **30**, 1187–1204. ISSN: 1573-0824. <https://doi.org/10.1007/s11045-018-0602-4> (2019).
 34. Dumble, S. J. & Gibbens, P. W. Horizon Profile Detection for Attitude Determination. *Journal of Intelligent & Robotic Systems* **68**, 339–357. ISSN: 1573-0409. <https://doi.org/10.1007/s10846-012-9684-7> (2012).
 35. Cornall, T. D., Egan, G. K. & Price, A. Aircraft attitude estimation from horizon video. *Electronics Letters* **42**, 744–745 (2006).
 36. Ettinger, S. M., Nechyba, M. C., Ifju, P. G. & Waszak, M. Towards flight autonomy: Vision-based horizon detection for micro air vehicles in Florida Conference on Recent Advances in Robotics **2002** (2002).
 37. Fefilatyeu, S., Smarodzinava, V., Hall, L. O. & Goldgof, D. B. Horizon Detection Using Machine Learning Techniques in 2006 5th International Conference on Machine Learning and Applications (ICMLA'06) (2006), 17–21. <https://doi.org/10.1109/ICMLA.2006.25>.
 38. Kristan, M., Kenk, V. S., Kovačič, S. & Perš, J. Fast Image-Based Obstacle Detection From Unmanned Surface Vehicles. *IEEE Transactions on Cybernetics* **46**, 641–654. ISSN: 2168-2275. <https://doi.org/10.1109/TCYB.2015.2412251> (2016).
 39. Hung, Y.-L., Su, C.-W., Chang, Y.-H., Chang, J.-C. & Tyan, H.-R. Skyline localization for mountain images in 2013 IEEE International Conference on Multimedia and Expo (ICME) (2013), 1–6.
 40. Liu, W.-H. & Su, C.-W. Automatic Peak Recognition for Mountain Images in *Advanced Technologies, Embedded and Multimedia for Human-centric Computing* (eds Huang, Y.-M., Chao, H.-C., Deng, D.-J. & Park, J. J. H.) (Springer Netherlands, Dordrecht, 2014), 1115–1121. ISBN: 978-94-007-7262-5.
 41. Zhang, H., Luo, Y., Qin, F., He, Y. & Liu, X. Elsd: Efficient line segment detector and descriptor in Proceedings of the IEEE/CVF International Conference on Computer Vision (2021), 2969–2978.
 42. Von Gioi, R. G., Jakubowicz, J., Morel, J.-M. & Randall, G. LSD: A Fast Line Segment Detector with a False Detection Control. *IEEE Transactions on Pattern Analysis and Machine Intelligence* **32**, 722–732. ISSN: 1939-3539. <https://doi.org/10.1109/TPAMI.2008.300> (2010).
 43. Akinlar, C. & Topal, C. EDLines: A real-time line segment detector with a false detection control. *Pattern Recognition Letters* **32**, 1633–1642. ISSN: 0167-8655. <https://doi.org/10.1016/j.patrec.2011.06.001> (2011).
 44. Hashmani, M. A. & Umair, M. A Novel Visual-Range Sea Image Dataset for Sea Horizon Line Detection in Changing Maritime Scenes. *Journal of Marine Science and Engineering* **10**. ISSN: 2077-1312. <https://doi.org/10.3390/jmse10020193> (2022).
 45. Zardoua, Y. et al. A Horizon Line Annotation Software for Streamlining Autonomous Sea Navigation Experiments. *Adv. Artif. Intell. Mach. Learn.* **3**, 1768–1786 (2023).
 46. Harris, C. R. et al. Array programming with NumPy. *Nature* **585**, 357–362 (2020).

-
47. Bradski, G. & Kaehler, A. OpenCV. *Dr. Dobb's journal of software tools* **3**, 2 (2000).